Hindawi
Journal of Nanomaterials
Volume 2022, Article ID 1790787, 13 pages
https://doi.org/10.1155/2022/1790787

Research Article

Application of Carbon Nanocomposite Sensing and Functional Magnetic Nanomaterial in the Sports Industry and Its Biosecurity Research

Zhenpeng Li,[1] Zhigan Li,[2] and Zecheng Zhang[3]

[1]*Sports Group, Zhongshan Yangxianyi Middle School, Zhongshan, 528403 Guangdong, China*
[2]*Department of Sports Medicine, Guangzhou Sport University, Guangzhou, 510075 Guangdong, China*
[3]*Sports College, Hainan University, Haikou, 570228 Hainan, China*

Correspondence should be addressed to Zecheng Zhang; 991913@hainanu.edu.cn

Received 25 January 2022; Revised 2 April 2022; Accepted 21 April 2022; Published 12 May 2022

Academic Editor: Awais Ahmed

Nanomaterial science is a particularly important research field in modern science and technology, which has attracted wide attention and research from all walks of life since its inception and has formed a relatively perfect category of science and technology. The purpose of this paper is to explore the application of carbon nanocomposite sensing and functional magnetic nanomaterial in the sports industry and their biosecurity research. This paper first discusses the research progress of nanocomposite in biosecurity and concludes that chemical modification can reduce the negative biological effects of nanomaterial, then puts forward the research methods on nanocomposite in the sports industry, and then selects nanosilver composites to explore and study the effects of different particle sizes and concentrations on the antibacterial properties of Aspergillus and test and characterize the properties of nanocomposite. The stability of nanocomposite modification electrodes is also explored. The results show that nanosilver has excellent bactericidal effects on both AF293 and Gra04. In particular, 8.08×10^{-5} mol/L and 4.03×10^{-5} mol/L nanosilver has a bacteriological rate of 100%, indicating that the growth of all fungal spores can be completely inhibited, and when the content of 10 wt% is found, the thermal conductivity of PHBE-MWNT pressure-sensitive composite materials is achieved 0.6975 W/(m-K), 1.8 times the MWNT pressure-sensitive glue, higher than the pure pressure-sensitive glue about 255%.

1. Introduction

Microorganisms are beneficial and harmful to human survival. The secondary metabolites of many bacterial species are antibiotics that are very useful for human diseases, and because of the short growth cycle and rapid reproduction of microorganisms, they are used in genetic breeding, which is of great significance. At the same time, microorganisms can also lead to the prevalence of infectious diseases, and 50% of human diseases are caused by viruses. Some microorganisms are spoilage, that is, cause undesirable changes in food odor and tissue structure. The evolutionary history of human society is the history of giving full play to the advantages of favorable bacteria to improve one's own life and to improve the quality of life by solving harmful bacteria. When the size of the material is reduced to a nanoscale, there will be some unique and interesting phenomena that cannot be observed in macromaterials, but these phenomena have not been found in the macrorange. Material scientists have discovered many materials with this phenomenon, such as quantum stimulation limits (quantum dots) for inorganic semiconductor nanomaterial, ultra-submagnetic (SPIONS) for iron oxide nanoparticles and localized surface plasma resonance (LSPR), for precious metal nanoparticles. It is an exciting task to solve practical problems by using the special properties of nanomaterial. The characteristics

of nanomaterials mainly include surface and interface effects, small size effects, quantum size effects, and macroscopic quantum tunneling effects.

To explore all aspects of nanocomposites, because of their smallness, they are not conducive to experimental exploration, but also because of their smallness, so nanocomposites are explored, so that it can provide reliable help not only in microbial research but also for clinical medicine and disease early warning of biomolecule detection methods which provide an important reference.

According to the research progress at home and abroad, different scholars have also made corresponding investigations in the research of carbon nanocomposite material sensing and functionalized magnetic nanomaterial: Zhao et al. conducted laboratory research on the performance of nanocarbon/copolymer SBS/rubber powder composite modified asphalt and chose nanocarbon particles modified by titanate coupling agent as the modifier. The morphology, microstructure, and surface properties of the prepared nanocomposite adsorbent were measured and analyzed by FESEM, TGA, XRD, FT-IR, and zeta potential. Batch experiments on the adsorption of Cr (VI) were carried out to determine the adsorption performance of the composites [1]. Wang et al.'s chemically synthesized conductive nanocomposites consisting of poly (PPy) are compared to components such as Cdots or PPy. It shows higher conductivity. The conductive film of this composite material is used for high sensitivity and selective detection of bitter acids in water and soil. This is the first report on conductivity-based sensing applications for Cdot nanocomposite, as opposed to traditional fluorescence-based sensing methods [2]. Pal et al. studied the composite modified asphalt prepared by Cdots and the high-speed shearing method for nanocarbon/copolymer SBS/rubber powder, used in extended tests, softening point tests, permeability tests, dynamic shear rheometer (DSR) tests, and curved beam rheometer (BBR) tests to evaluate physical performance [3]. Jiang et al. have produced a diamond-like carbon (G/a-C:H) nanocomposite film mixed with graphene by liquid phase electrochemical method. The growth mechanism of the nanocomposite membrane is proposed and discussed. The deposited coating material was measured using scanning electron microscopy (SEM), Raman spectroscopy, spread electron microscopy (TEM), and Fourier transform infrared (FTIR) spectra. The results show that graphene sheets are evenly dispersed in the hydrogenated amorphous carbon (a-C:H) matrix [4]. Xu and Zhang have developed an easy preparation method for nanocomposite consisting of graphene oxide and manganese dioxide nanowires (GO/MnO2NWs). The basic form, structure, and composition of the resulting substance are characterized by a transmission electron microscope, X-ray diffraction, and N2 adsorption and desorption [5]. Hien et al. have successfully developed an effective electrochemical method for the production of poly phenylamine/multiwall carbon nanotube nanocomposite on the fork-finger platinum microelectrics to improve biosensor performance. The shape and properties of nanocomposite were studied through field emission scanning electron microscopes and ultraviolet visible spectra [6]. Amir et al.'s study discusses the effects of effective functionalization on signal sensitivity observed on 6-TG electrooxidation on CA-Fe3O4 NPs, with the use of bare and niacin (NA) functional Fe3O4 NP modified glass carbon electrode compared. The experimental results provide sufficient evidence to support the importance of favorable functions for achieving higher signal sensitivity of 6-TG electrooxidation [7]. Cao et al. studied the prepared ZnONR sensors, MWCNT sensors, and ZnONR/MWCNT ethanol gas sensitivity of nanocomposite gas sensors. ZnONR/MWCNT nanocomposite sensors exhibit higher response, faster response recovery, and better ethanol selectivity than ZnONR and MWCNT sensors [8]. However, these studies have not combined the application of sports industry and its biological safety to make some progress.

The innovative focus of this paper is mainly reflected in the following: (1) the paper introduces the research on biosecurity of nanocomposite and concludes that chemical modification can reduce the negative biological effects of nanomaterials and puts forward research methods based on nanocomposite in the sports industry. (2) The performance of nanocomposite is analyzed from a biological point of view, and the properties of nanocomposite are tested and characterized, and the stability of nanocomposite modified electrodes is explored.

2. Methods in Biosecurity and Sports for Nanocomposite

2.1. Biosecurity in Nanocomposite. Due to the industrialization of nanotechnology, people's daily life and occupation with nanomaterial contact are increasingly frequent, so the use of nanomaterial on the body and the environment may also cause more attention. Some of the nanoparticles newly created by engineering science may be cancer-causing. Researchers found that fish developed brain cancer after ingesting small amounts of carbon nanomaterials. Laboratory mice developed symptoms of lung disease after inhaling carbon nanotubes, as if they had inhaled asbestos particles. So far, the study of the biological effects of nanomaterial is still in its infancy, and scientists have only made preliminary studies on the biological effects of carbon-based nanomaterial and metals and their oxide nanomaterial [9]. When a biological material exceeds the nanosize (1-100 nm), it has a very good surface area due to its size close to the biological atomic scale, allowing it to interact directly with individual biological atoms [10]. Nanomaterials show the good electronic, optical, magnetic, mechanical, and other properties inherent in nanoscale, making it more sensitive to the surrounding environment and the target molecules in the sample, which is conducive to detection. Nanoelectrochemical sensors made from these nanomaterials have achieved some results in simplifying the detection process, improving sensitivity, reducing detection limits, and reducing costs, as shown in Figure 1.

The biological effects of nanomaterial are closely related to their physical and chemical properties, biological cells are at micron scale, and nanomaterials extremely easily enter into biological cells and interact with them, thus affecting

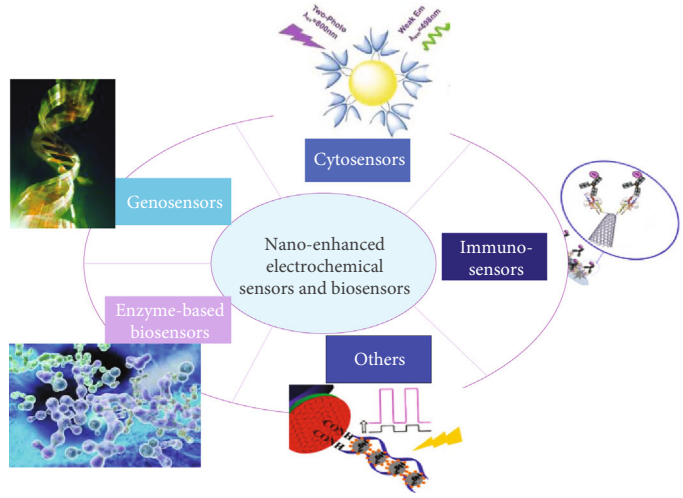

Figure 1: Schematic diagram of electrochemical sensors and biosensors based on nanomaterial and nanostructures.

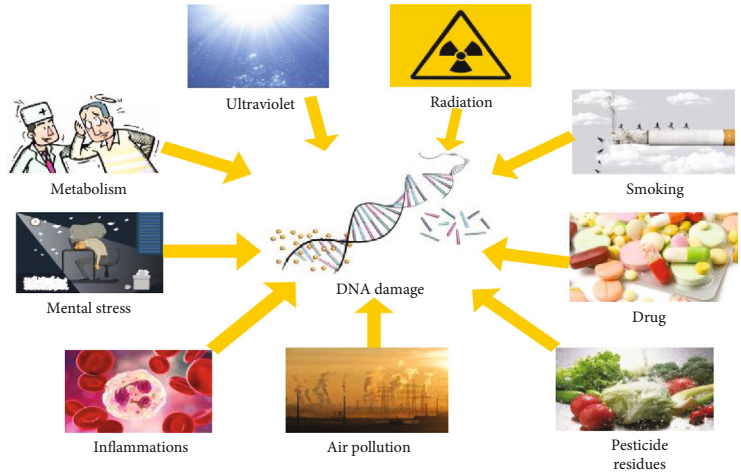

Figure 2: Factors affecting biological damage.

biological functions [11]. Figure 2 represents the factors that affect biological damage. Because of their small size, these tiny factors are difficult to detect, and they are quietly hidden around us, which will slowly erode our bodies. Scientific studies have confirmed that some micron-scale compounds that appear in the form of stable clusters are nontoxic, but when they are heated into smaller-scale nano- or ultra-microlevel particles, they can also show some toxicity, such as having rats contain 20 nm of PFC (PTEF). Nanoparticles breathe 15 min in the air, and most rats die within the next 4 hours, instead containing 130 nm PTEF. Rats breathing in the air did not see discomfort [12].

The biological effects of nanomaterial are not only influenced by particle size but are also closely related to their structure. With the quantitative change of particle size, the qualitative change of particle properties will be caused under certain conditions. The change in macroscopic physical properties due to particle size reduction is called the small size effect. For ultrafine particles, the size becomes smaller and the specific surface area increases significantly, resulting in a series of novel properties as follows. The study found that tubular structure carbon nanomaterials (MWCNTs) and onion-like carbon nanomaterial (MWCNO) in the same dose and in the same size range showed different toxic effects and mechanisms on human fibroblasts. MWCNTs cause a strong immune and inflammatory response from fibroblasts in the human skin, while MWCNO is a genetically induced response of fibroblasts to external stimuli [13]. The cytotoxicity of single-walled carbon nanotubes (SWNTS), multiwall carbon nanotubes (MWNT10), and fullerene (C60) to alveolar macrophages was then compared; its cytotoxicity from strong to weak isSWNTS > MWNT10 > C60; for SWNTS concentration of 11.30 μg/cm^2 at a concentration of 22.6 μg/cm^2, there was significant cytotoxicity, while for C at a concentration of 226 μg/cm^2, there is still no significant cytotoxicity [14]. It has also been reported that surface-derived treatment of C60 reduces nanotoxicity to human epidermal cells (HDFs) by 100,000 times, showing that chemical modification can reduce the negative biological effects of nanomaterial.

At present, there is no unified international evaluation criterion on the biological stability of nanomaterial [15].

Nanomaterial can interfere with endogenous metabolism or signal transduction pathways in a very weak way, thus disrupting the biochemical function of cells, and the results are difficult to show in short-term toxicity analysis. Therefore, when evaluating the biological efficacy of nanomaterial using short-term or subchronic experiments, a representative in vivo or in vitro environment should be used, a negative and positive control group should be set up, and the entire experimental process should be calibrated [16].

2.2. Methods on Nanocomposite Materials in the Sports Industry

(1) Factor analysis and spatial effects

Factor analysis is an analytical method that uses the idea of "low dimension" to extract a few representative factors from many original variables [17]. The KMO test statistic is an indicator used to compare simple and partial correlation coefficients between variables. It is mainly used in factor analysis of multivariate statistics, which can also be used to study the similarity between variables in multifactor analysis. The mathematical concept of KMO test statistics is as follows:

$$\mathrm{KMO} = \frac{\sum\sum_{m\neq n} t_{mn}^2}{\sum\sum_{m\neq n} t_{mn}^2 + \sum\sum_{m\neq n} u_{mn}^2}, \tag{1}$$

where t_{mn} is a simple correlation coefficient between a variable a_m and a_n other variables, u_{mn}, and a partial correlation coefficient between a variable and a variable that a_m controls the a_n remaining variables. As can be seen from the formula (1), KMO statistics range from 0 to 1. The closer the KMO value is to 1, the stronger the correlation between the variables, and the more suitable the original variable is for factor analysis [18]. The closer the KMO value is to 0, the weaker the correlation between the original variables, and the less suitable the original variable is for factor analysis [19].

Once the KMO test has passed, factor analysis is possible. The mathematical model of factor analysis is as follows.

With the original g variables, $L_1, L_2, L_3, \cdots, L_g$, and all of which have been standardized, each variable can be $i (i < g)$ represented by a linear combination of $D_1, D_2, D_3, \cdots, D_i$ factors, as follows:

$$\begin{cases} L_1 = k_{11}D_1 + k_{12}D_2 + \cdots + k_{1i}D_i + \omega_1, \\ L_2 = k_{21}D_1 + k_{22}D_2 + \cdots + k_{2i}D_i + \omega_2, \\ \cdots \\ L_g = k_{g1}D_1 + k_{g2}D_2 + \cdots + k_{gi}D_i + \omega_g. \end{cases} \tag{2}$$

Formula (2) can also be expressed as a matrix, $L = KD + \omega$, where D is a common factor; K is a load matrix of factors and is a factor load, $k_{mn} (m = 1, 2, \cdots, g; n = 1, 2, \cdots, i$ representing the first m load of the original variable on the nth common factor; ω is a special factor, which is the part of the original variable that cannot be interpreted by the public factor, with an average value of 0.

Then, construct the weight function, mainly by using the variance contribution rate of each common, and then, get the comprehensive evaluation function; the formula is as follows:

$$D = \sum_{m=1}^{e} \sigma_m D_m, \tag{3}$$

where $\sigma_m = \varphi_m / \sum_{m=1}^{e} \varphi_s$ indicates the weight of the ith measurement factor.

Spatial relevance is when a region's behavior or phenomenon affects an adjacent region; i.e., features with similar behavior or phenomena are spatially brought together [20]. Therefore, there is a functional relationship d between the observation variable of the ith w_{tm} space observation unit and the observation variable of its adjacent region. Its general expression is

$$w_m = d(w_1, \cdots, w_{m-1}, w_{m+1}, \cdots, w_t) + \omega_m, \quad m = 1, \cdots, t, \tag{4}$$

in the formula, representing ω_m random interference items.

Spatial structure heterogeneity, also known as spatial structure inconsistency and spatial structure differences, is determined by the spatial structure measurement mode of the second main source of spatial structure efficiency [21]. Spatial heterogeneity shows the characteristics of events or phenomena in different regions of the space environment [22]. Spatial heterogeneity can be expressed as

$$q_a = g_a(p_a, \varphi_a, \sigma_a). \tag{5}$$

a represents the space observation unit, $a = 1, \cdots, i$. g_a is the function relationship between q_a-dependent variables and p_a arguments, parameter variables, φ_a and random interference items σ_a.

Typically, a linear relationship is described as follows:

$$q_a = P_a \varphi_a + \sigma_a \tag{6}$$

in formula represents the P_a vector used to interpret the variable, represents the parameter vector that the φ_a explanatory variable has an effect q_a, is the q_a explanatory variable that represents the observation of a region, and is a random σ_a interference term.

Global spatial self-correlation can measure the self-correlation between regions in the overall research space. Common domain-wide spatial self-correlation metrics are Global Moran's I statistics, assuming a vector, described as follows:

$$I = \frac{\sum_{a=1}^{m}\sum_{b=1}^{m} u_{ab}(t_a - \bar{t})(t_b - \bar{t})}{\sum_{a=1}^{m}\sum_{b=1}^{m} u_{ab}\sum_{a=1}^{m}(t_a - \bar{t})^2} = \frac{\sum_{a=1}^{m}\sum_{b=1}^{m} u_{ab}(t_a - \bar{t})(t_b - \bar{t})}{D^2\sum_{a=1}^{m}\sum_{b=1}^{m} u_{ab}}. \tag{7}$$

m is the total number of regions in the study area, the u_{ab} spatial weight; t_a and t_b are the properties of regions a and b,

respectively; $\bar{t} = (1/m)\sum_{a=1}^{m} T_a$ is the average of the property; $D^2 = (1/m)\sum_{a=1}^{m}(t_a - \bar{t})^2$ is the variance of the property.

When the Global Moran I index is measured, it is also tested, usually using the X test the formula as follows:

$$X = \frac{M - F(M)}{\sqrt{U(M)}}. \tag{8}$$

Among them,$F(M)$is the theoretical mean and$U(M)$is the theoretical standard deviation.

Essentially, the Local Moran I index is a decomposition of Global Moran's I, a global spatial autocorrelation statistic. For the ith region, it takes the form of

$$I_a = \frac{m^2}{\sum_a \sum_b u_{ab}} \times \frac{(t_a - \bar{t})\sum_b u_{ab}(t_b - \bar{t})}{\sum_b (t_b - \bar{t})^2}. \tag{9}$$

The Local Moran I index is tested similar to the global index.

(2) Linear regression model in sport

In practice, there are often many factors that influence a phenomenon, so multiple regression analysis methods are often used to study the interaction between a variable and many variables [23]. In practical problems, the establishment of a multiple regression model can analyze complex problems in a diversified manner, making them easier to understand, so as to solve the problem. A multilinear regression model can be formed when there is a linear association between the resolved variable and the resolved variable. The usual form of a multilinear regression model is

$$y = \varphi_0 + \varphi_1 x_1 + \varphi_2 x_2 + \cdots + \varphi_n x_n + \delta, \tag{10}$$

where it is called a dependent variable and is called an$x_1, x_2, \cdots, x_n$argument; $\varphi_1, \varphi_2, \cdots, \varphi_nisn$plus 1 argument to be evaluated, is a constant, is φ_0 a regression parameter, and is a random $\varphi_1, \varphi_2, \cdots, \varphi_n\delta$error.

The GWR model can be represented as

$$f_a = \partial_0(s_a, t_b) + \sum_{b=1}^{h} \partial_b(s_a, t_b) x_{ab} + \varphi_a, \quad a = 1, 2, \cdots, m. \tag{11}$$

(s_a, t_b) is the spatial coordinate of the first sample point, $\partial_b(s_a, t_b)$, and the bth regression factor of the a sample point is a random error φ_a term. For ease of expression, you can shorthand the above as

$$f_a = \partial_0 + \sum_{b=1}^{j} \partial_{ab} x_{ab} + \varphi_a, \quad a = 1, 2, \cdots, m. \tag{12}$$

If $\partial_{1b} = \partial_{2b} = \cdots = \partial_{mb}$, the GWR model then becomes a normal linear regression model.

Further, based on "data that is farther away from the observation data closer to position i has a greater impact on the estimate," the GWR model parameters can be estimated using weighted least squares:

$$\widehat{\partial}(s_a, t_b) = \left(C^E U(s_a, t_b) C\right)^{-1} C^E U(s_a, t_b) F, \tag{13}$$

where $\widehat{\partial}$ is the estimate of ∂, m is the number of spatial sample points,$b$is the number of arguments,U_{am}, and the position; a depiction model is given to the data point, the weight of m, which is the corresponding spatial$U(s_a, t_b)$ weight matrix.

How to select the appropriate threshold L is the key to the distance threshold method. The distance between data point$b$ and regression point a is recorded as l_{ab} comparing the l_{ab} value to L; if l_{ab} is greater than L, the weight is 0, otherwise 1; the formula is as follows:

$$U_{ab} = \begin{cases} 1 & l_{ab} \le L, \\ 0 & l_{ab} > L, \end{cases} \tag{14}$$

where spatial relationships are measured by distance:

$$U_{ab} = \frac{1}{l_{ab}^{\alpha}}. \tag{15}$$

In the upper class, α is the appropriate constant, generally with a value of 1 or 2, which corresponds to the square of the distance countdown and the distance countdown, respectively.

The continuous monotony decreasing function is used to reveal the correlation between distance and weight, in which Gauss function method is a more common function; the specific formula is as follows:

$$U_{ab} = \exp\left(-\left(\frac{l_{ab}^{\alpha}}{k}\right)^2\right). \tag{16}$$

k is a nonnegative attenuation parameter that illustrates the correlation between weights and distance coefficients and is also called bandwidth. It can be found by the formula sub (16); the larger the broadband k, the lower the rate of weight decay with the increase of distance. If the broadband k is smaller, the rate of weight decay increases as the distance increases, as does Figure 3 for the Gauss spatial right function.

In practice, data points that have little effect on regression parameters are usually cut off and do not participate in the calculation [24]. In this case, the Gauss function is replaced by a finite Gaussian function, which is the most commonly used method.

$$U_{ab} = \begin{cases} \left[1 - \left(\frac{l_{ab}}{k}\right)^2\right]^2 & l_{ab} \le k, \\ 0 & l_{ab} > k. \end{cases} \tag{17}$$

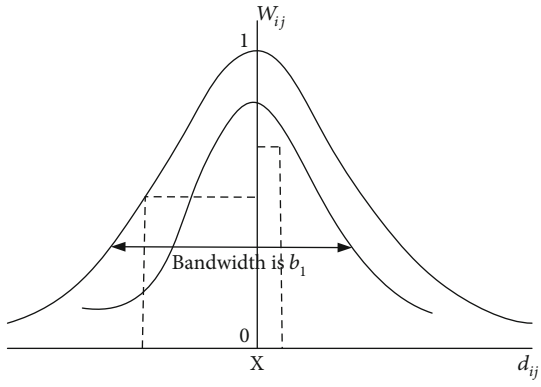

Figure 3: Gauss space weight function.

Akaike also made improvements to the parameter estimation method of the greatly similar principle, and on this basis, a more general mode l selection criterion, namely, Akaike information criteria, is given. The AIC guidelines are defined as

$$\mathrm{AIC} = -2lnH\left(\widehat{\delta}_H, x\right) + 2r. \tag{18}$$

Among them,$\widehat{\delta}_H$is for a very similar estimate and$r$is the number of unknown parameters.

AIC guidelines are widely used in practice. In the early days, the AIC criterion was applied to nonparametric regression analysis to select smooth parameters, the formula being

$$\mathrm{AICc} = 2mln\left(\widehat{\theta}\right) + mln(2\pi) + m\frac{m + tr(T)}{m - tr(T)}. \tag{19}$$

Here, AICc represents the "modified" AIC estimate and$m$is the size of the sample point, represents the standard distance between the random error term and the estimate, represents the trace of the GWRTmatrix, and is a function of bandwidth. The value of the AIC can also be used to judge whether GWR modeling is better than OLS modeling.

To find out how to choose the best bandwidth method, cross-validation is recommended, which is based on local regression analysis, the formula of which is represented as follows:

$$CV = \sum_{a=1}^{m}\left[f_a - \widehat{f}_{\neq a}(m)\right]^2, \tag{20}$$

where$\widehat{f}_{\neq a}(b)$is the sum value off_a; i.e., the observation of point$a$itself is deleted when fitting. This way, when bandwidth m becomes very small, the model only fits near regression point a, included in bandwidth m. Sample points in the range do not include a itself [25]. The smaller the CV value, the better the model fits. In the actual calculation, in order to select the optimal bandwidth m and its CV value, you can select multiple bandwidths b at the calculation and measure their CVs separately value to find the best result. The application of carbon nanocomposite sensing and functional magnetic nanomaterial in the sports industry is studied in Figure 4 [26–28].

3. Experimental Results of Carbon Nanocomposite Sensing and Functional Magnetic Nanomaterial in Biosecurity Research

3.1. Exploration of Nanosilver Composites of Different Particle Sizes and Concentrations in the Biological Field. In order to analyze the performance of nanocomposites from a biological point of view, this paper selects nanosilver composites to explore and study the effects of their different particle sizes and concentrations on the antibacterial properties of aspergillosis [29].

(1) Effects of different particle sizes on the antibacterial properties of Aspergillus AF289

Table 1 shows the results of the experiment showing the same concentration (12.12×10^{-5} mol/L) of nanosilver solution; at 10 nm to 40 nm, the antibacterial effect in the particle size range is very significant, especially 10 to 25 nm. Nanosilver antibacterial rate reached 80%, so the antibacterial effect on fungal spores under this particle size is most obvious.

(2) Effects of different particle sizes on the resistance of the drug-resistant bacteria Gra04 to aspergillation

In Table 2, experimental results show the same concentration (12.12×10^{-5} mol/L) of nanosilver solution; at 10 nm to 40 nm, the antibacterial effect in the particle size range is very significant, especially the nanosilver antibacterial rate of 10 to 25 nm that reached 80%, so the antibacterial effect on fungal spores is most obvious under this particle size.

(3) Effects of different concentrations on the antibacterial properties of aspergillosis AF293

As can be seen from Table 3, different concentrations of nanosilver have different antibacterial activities against AF293 of pentomycin. In experiments with the same particle size, nanosilver series dilution concentration, in the range of 2.02×10^{-5} mol/L to 16.16×10^{-5} mol/L nano-silver has a significant antibacterial effect, especially 8.08×10^{-5} mol/L and 4.03×10^{-5} mol/L. The bacteriostatic rate reached 100%, indicating that the growth of all fungal spores could be completely inhibited [30].

(4) Effects of different concentrations on the resistance of Gra04, a drug-resistant bacteria of aspergillation

In Table 4, the experimental results show that different concentrations of nanosilver have different antibacterial activities against the drug-resistant bacteria Gra04 of penicillin. In experiments with the same particle size nanosilver series dilution concentration, in the range of 2.02×10^{-5} mol/L to 16.16×10^{-5} mol/L, nanosilver has a significant

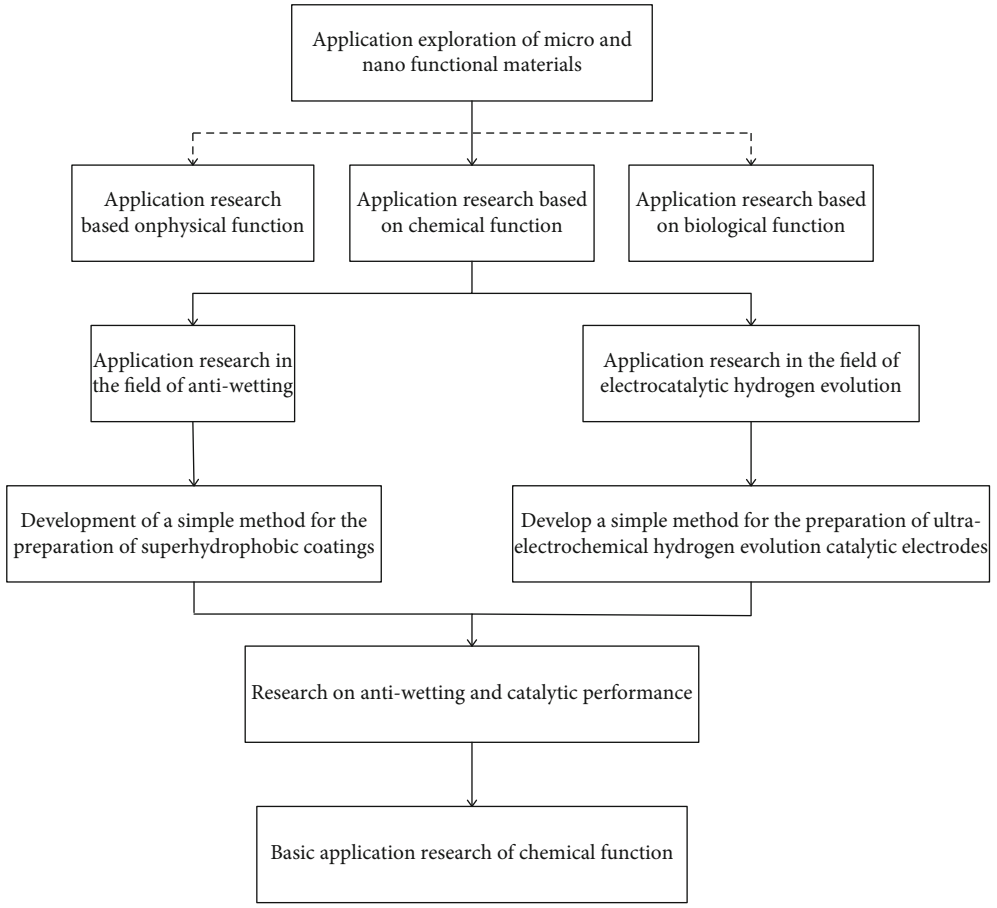

Figure 4: Main technical route.

Table 1: Determination of the antibacterial rate of Aspergillus fumigatus AF289 with different particle diameters of nanosilver.

AgNPs (10^{-5} mol/L)	Examples of experiments		Total colonies (cfu/mL)	Antibacterial rate (%)
	1	2		
10~15 nm	11	8	19	79
20~25 nm	9	9	18	78
30~40 nm	13	5	18	68
Control	39	51	90	

Table 2: Determination of the antibacterial rate of nanosilver with different particle diameters on the resistant bacteria Gra04 of Aspergillus fumigatus.

AgNPs (10^{-5} mol/L)	Examples of experiments				Total colonies (cfu/mL)	Antibacterial rate (%)
	1	2	3	4		
10~15 nm	61	62	21	20	151	80
20~25 nm	59	69	11	9	149	81
30~40 nm	19	6	81	67	166	76
Control	159	168	158	169	669	

Table 3: Determination of the antibacterial rate of Aspergillus fumigatus AF293 with different concentrations of nanosilver.

AgNPs (10^{-5} mol/L)	Examples of experiments		Total colonies (cfu/mL)	Antibacterial rate (%)
	1	2		
15.15	31	26	57	39
11.11	9	8	17	80
7.07	0	0	0	100
3.03	0	0	0	100
1.01	9	6	15	79
Control	39	45	84	

Table 4: Determination of the antibacterial rate of different concentrations of nanosilver to the resistant strain Gra04 of Aspergillus fumigatus.

AgNPs (10^{-5} mol/L)	Examples of experiments				Total colonies (cfu/mL)	Antibacterial rate (%)
	1	2	3	4		
15.15	160	168	109	131	566	18
11.11	49	61	21	20	151	80
7.07	0	0	0	0	0	100
3.03	0	0	0	0	0	100
1.01	26	19	0	0	45	92
Control	159	169	158	168	654	

antibacterial effect, especially 8.08×10^{-5} mol/L and 4.03×10^{-5} mol/L. The bacteriostatic rate reached 100%, indicating that the growth of all fungal spores could be completely inhibited.

3.2. Performance Testing and Characterization of Nanocomposites. The tensile strength and thermal conductivity of PSA, MWNT/PSA, and DABP-MWNT/PSA composites are tested with electronic pullers and thermal coefficients, as shown in Figure 5.

As can be seen from Figure 5, the stretch strength of the decompression carbon nanotubes of DABP liquid crystal is more significant than that of the undefined carbon nanotubes. The maximum tensile strength of pure pressure-sensitive adhesive is 0.5048 MPa, and the pressure-sensitive adhesive nanocomposite is produced with MWNT and DAP-MWNT technology, respectively, and the maximum tensile strength of pressure-sensitive adhesive composites will be significantly increased due to the increase of nanoparticle concentration, and for DABP-MWNTs/under different nanoparticle contents, the tensile strength of the pressure-sensitive composite is greater than that of the MWNT/pressure-sensitive composite. When the MWNT content is 2 wt%, the DABP-MWNT/pressure-sensitive composites have a tensile strength of 14.19 MPa, which is greater than MWNTs. The 1.914 MPa of pressure-sensitive composites is approximately 641% higher than pure pressure-sensitive composites, approximately 27 times higher than pure pressure-sensitive adhesives. In the description of carbon nanotubes due to defects such as easy reunion and poor compatibility with pressure-sensitive adhesives, its excellent mechanics have been unachievable, and the effect of improving the properties of pressure-sensitive adhesives is not obvious, and the carbon nanotubes have been functionalized by DABP liquid crystals because DABP and MWNTs combine to π-π interactions, the reunion of carbon nanotubes inhibited the dispersion, and compatibility of carbon nanotubes in pressure-sensitive adhesives is improved, which makes the dynamics of pressure-sensitive adhesive composites significantly improved [26]. In addition, if the concentration of nanoparticles is further increased, the pressure-sensitive adhesive complex required in the mold will not be formed, so the maximum concentration of nanoparticles in the pressure-sensitive adhesive complex that detects the dynamic properties is 2.0 wt%.

It can be found from the figure that the thermal conductivity of pure pressure-sensitive adhesives is only 0.1965 W/(m-K), which has been modified by MWNTs and DABP-MWNTs, and due to the increase in the concentration of nanoparticles, the thermal conductivity of pressure-sensitive adhesive complexes is further improved. Compared with carbon nanotubes that have not been functionalized by liquid crystals, DABP-MWNTs have a particularly strong effect on the thermal conductivity of pressure-sensitive adhesives. At various nanoparticle concentrations, the thermal conductivity of DABP-MWNT/pressure-sensitive adhesive composites is larger than that of MWNT/pressure-sensitive adhesive composites. This is due to defects such as the ease of reuniting of the carbon nanotubes themselves and poor compatibility with pressure-sensitive adhesives, which make their excellent thermal conductivity impossible, thus improving the thermal conductivity of pressure-sensitive adhesives without significant effect, but through

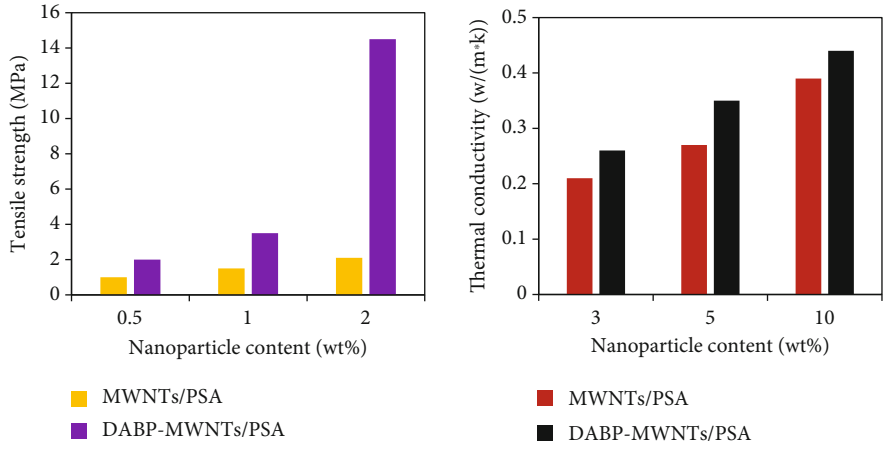

Figure 5: The influence of nanocomposite tensile strength and thermal conductivity.

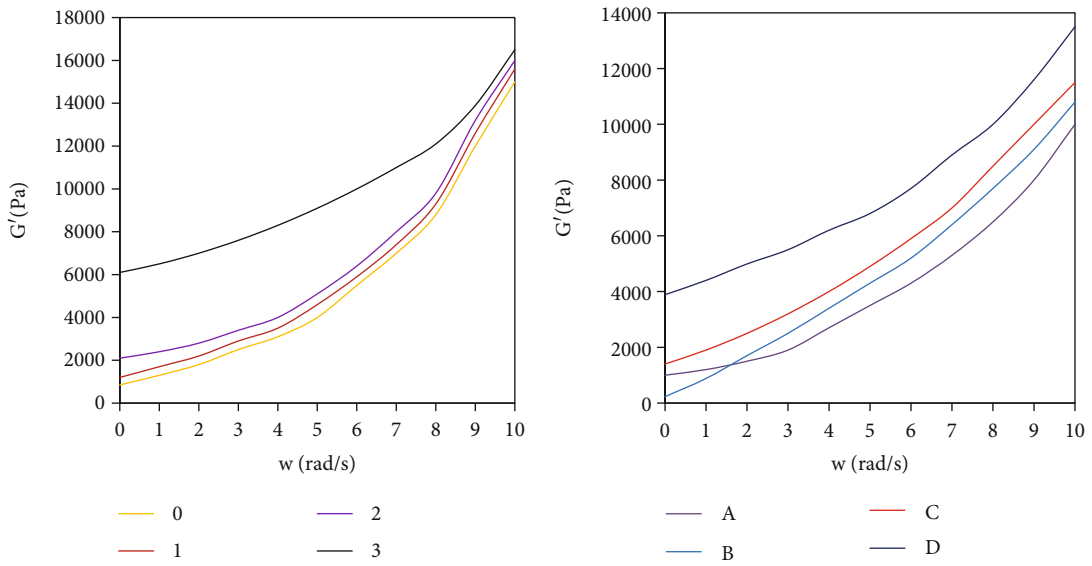

Figure 6: The relationship between storage modulus and scanning frequency.

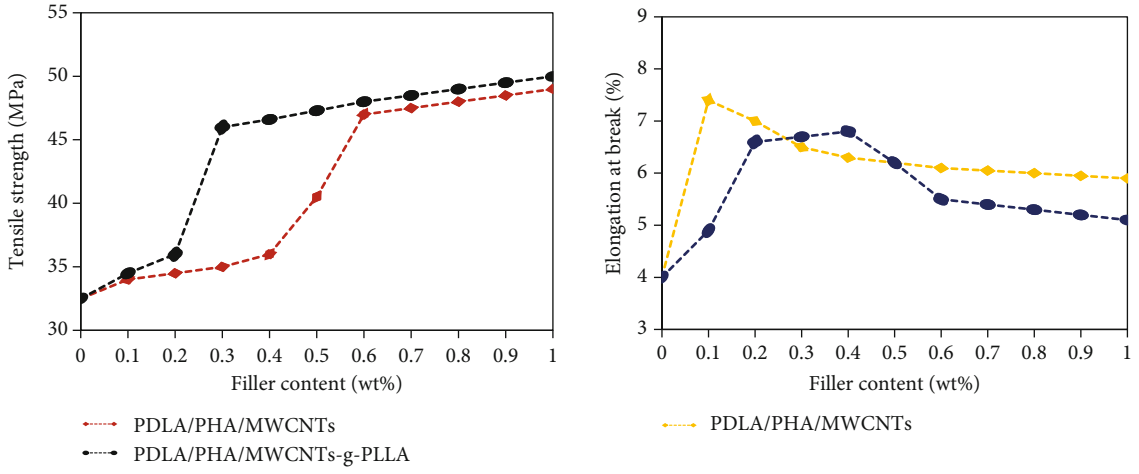

Figure 7: The relationship between mechanical properties and filler content.

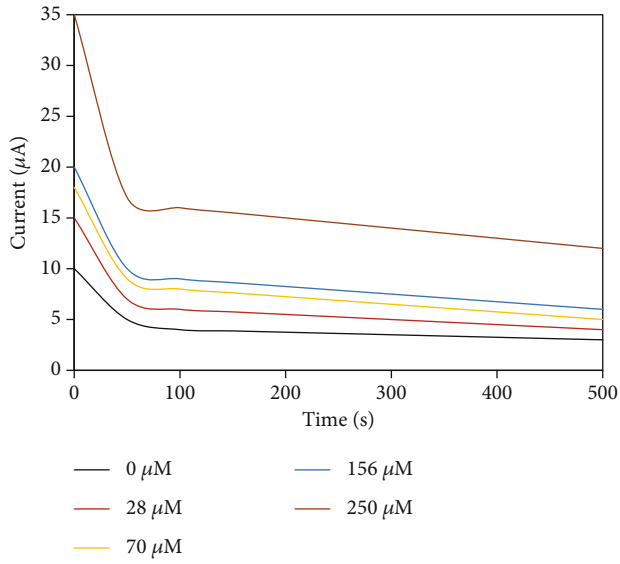

Figure 8: Chronoamperometry graph.

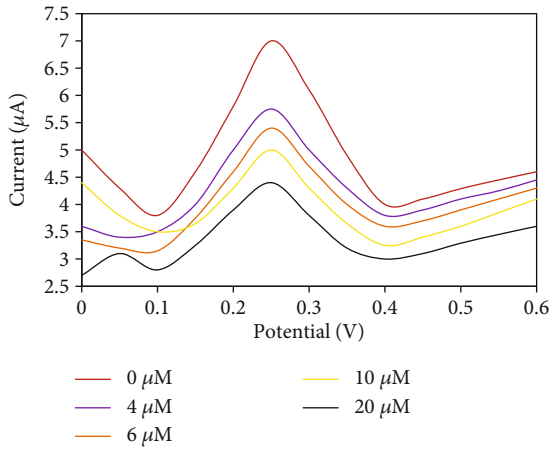

Figure 9: Differential pulse voltammograms.

DABP, the carbon nanotubes after the functionalization of liquid crystal have better dispersion and compatibility in the pressure-sensitive glue, which makes the thermal conductivity of the pressure-sensitive adhesive composite material improve greatly. When the content is 10 wt%, the thermal conductivity of the DABP-MWNT/pressure-sensitive composites reaches 0.4208 W/(m-K), which is MWNTs/1.1 times the pressure-sensitive glue, which is about 114% higher than the pure pressure-sensitive glue.

Rheological parameters such as storage modulus (G') are very useful in detecting the dispersion state of fillers, especially when forming the percolation network structure of anisotropic fillers. For PDLA/PHA/MWCNT and PDLA/PHA/MWCNT-g-PLLA nanocomposites at 180 degrees C in energy storage module$G'$and filler content, the graph of scan frequencies is shown in Figure 6. As can be seen from the figure, in the low-frequency region, MWCNTs tend to form a network structure in the PDLA substrate as the content of MWCNTs increases; as a result, the energy storage capacity of PDLA/PHA/MWCNT nanocomposites increases as well. When a platform appears in the low-frequency area of the energy storage module G' curve, it usually indicates the formation of a overseepage network. The energy storage modulus G' of PDLA/PHA mixture increases monotonically as the frequency of scanning increases, showing the end flow behavior of the viscous polymer melt. When the MWCNT content in PDLA/PHA/MWCNT nanocomposites is 0.6 wt%, the material appears in the low-frequency zone with energy storage modulus platform which indicates that the critical content of MWCNTs forming a network structure is 0.6 wt%. PDLA/PHA/MWCNT-g-PLLA nanocomposites show similar patterns of change. However, its rheological percolation content is lower, 0.4 wt%. The above results indicate that the rheological percolation network structure is the conductive percolation network structure.

Composite PHA in the material improves the brittleness of the PDLA while significantly reducing the tensile strength of the PDLA. It can be seen from Figure 7 that the tensile strength of PDLA/PHA blends increases with the increase of MWCNT content. When the content of MWCNTs increased from 0 wt% to 1.2 wt%, the tensile strength of PDLA/PHA/MWCNT and PDLA/PHA/MWCNT-g-PLLA nanocomposites increased from 32.1 MPa to 45.1 MPa and 50.2 MPa, respectively. However, there was no significant change in the fracture elongation of the two composites. It is worth noting that PDLA/PHA/MWCNT-g-PLLA nanocomposites are always more tensile than PDLA/PHA/MWCNT nanocomposites at the same filler content. This is because MWCNTs-g-PLLA is selectively dispersed in the substrate PDLA and has a large adhesion to the substrate's interface (building composites). The enhancement effect on the substrate is more significant. Based on the above discussion, the formation of MWCNT and MWCNT-g-PLLA networks can significantly enhance PDLA/PHA mixes, resulting in weak to strong transitions. In addition, this transition can be achieved by adding a small amount of MWCNTs-g-PLLA compared to MWCNTs. Once the nanofiller network is formed, the strength of the two nanocomposites will stabilize with the increase of nanofillers.

3.3. Stability of the Nanocomposite Modified Electrode. The stability of nanocomposites as electrodes is one of the important parameters to measure the quality of sensors. Timing current method is a kind of electrochemical method related to the function between the measurement of voltage response and current duration. When time tends to be infinite, the voltage will also be closer to zero as the content of surface active substances in the high-voltage electrode decreases gradually with electrolytic time. In this paper, the stability of modified electrodes is studied by the timing current method, as shown in Figure 8.

In this paper, the stability of modified electrodes is studied by timing current in different concentrations of TNP solutions. As the concentration of the TNP solution increases, the response current page for the modified electrode increases, and the current gradually stabilizes after approximately 50 seconds of timing, indicating that the

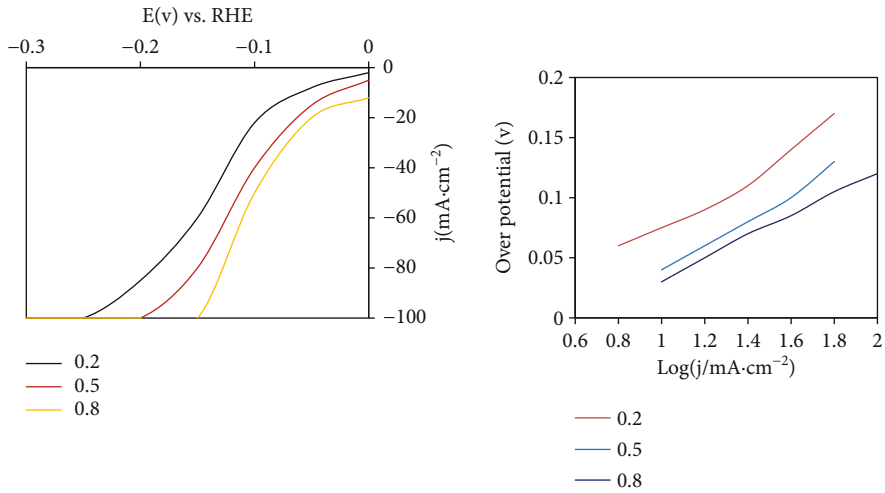

Figure 10: Hydrogen evolution catalytic performance graph.

prepared nanocomposite modified electrode pair TNP has good stability and electrocatalytic activity.

In addition, we use DPV as shown in Figure 9.

We immersed NQS/GO GCE in a 1.0 mM potassium iron cyanide solution and then added creatine to the solution continuously and examined the electrochemical behavior of different concentrations of creatinine on the electrodes. It can be seen from the figure that with the increase of creatinine concentration in the solution, the peak current decreases gradually. This is mainly due to the ability of creatinine to react with NQS on the electrode surface, causing the electrode surface to change, resulting in a gradual decrease in peak current.

The electrodeposition parameters, especially the sedimentary current density, have a significant effect on the hydrogenic catalytic properties of Co/CoP-NF catalysts. The catalysts produced were named Co/CoP-NF-2, Co/CoP-NF-5, and Co/CoP-NF-8. Figure 10 describes the hydrogenic catalytic properties of Co/CoP-NF-2, Co/CoP-NF-5, and Co/CoP-NF-8 catalysts. Obviously, the Co/CoP-NF-5 catalyst showed the highest hydrogenic catalytic activity, the hydrogen-based catalysis of Co/CoP-NF-8 was moderate, and the hydrogen-analysis catalysis of Co/CoP-NF-2 was the worst. The values of switching current density and hydrogen analysis performance are shown in Table 5, from which the Co/CoP-NF-5 catalyst has the highest exchange current density, further demonstrating that it has the highest hydrolytic catalytic activity.

Table 5: Co/CoP-NF catalyst HER performance parameters under different deposition current densities.

Deposition current	n_{10} (mV)	n_{100} (mV)	b (mV)	j_0 (mV)
0.3	81	209	101	1.69
0.6	38	129	69	2.99
0.9	39	171	102	2.79

4. Discussion

It is well known that nanosilver has a good killing property, against bacteria, fungi, mold, and other pathogens. Therefore, we have studied the nanosilver experiment to kill smoke and mold. Experimental results show that at concentrations of 4.04×10^{-5} mol/L, nanosilver-to-smoke mold with a particle size of 10 to 15 nm (drug-resistant and wild strains) is better killed. Therefore, nanosilver has a great prospect in the killing treatment of drug-resistant strains. In addition, nanosilver sterilization is likely caused by nanosilver damage to the integrity of the cell wall and cell membrane, resulting in the outflow of material from the cell. However, the most critical issue for nanosilver particles is biosecurity. It is now known that nanosilver is indeed toxic, so it is urgent to find the right dose and concentration of sterilization that are harmless to humans. At the same time, based on the mechanism of a pronuclear replacement reaction between organic matter NQS and creatine, a new method of creatine coloric testing based on NQS/GO nanocomposites is established. The sensing mechanism is proved by UV-vis and electrochemical techniques. Experimental results show that NQS can be combined with GO through π-π and can effectively improve the effectiveness of color detection. The absorbance of solvents and the added creatinine content has a good linear relationship within the specified content range. Direct visual sensing methods are simple, fast, sensitive, economical, and selective, so we do not need some sophisticated analytical instruments to achieve rapid detection. It provides an important reference for the detection of biomolecules in clinical medicine and disease early warning and a new method for exploring the principle of visual sensors.

5. Conclusions

Using the thermal conductivity factor instrument, the thermal conductivity of PSA, MWNT/PSA, and PHBE-MWNT/PSA composites was detected, and the results showed that after the transformation of MWNTs and PHBE-MWNTs, the thermal conductivity was increased,

and the thermal conductivity of pressure-sensitive adhesive composites was significantly improved due to the increase of nanoparticle concentration. Compared with nanotubes that have not been functionalized by liquid crystals, PHBE-MWNTs have improved their thermal conductivity in pressure-sensitive adhesives. This is due to the fact that PHBE and MWNTs can be combined with π-π interactions, inhibiting the unification of carbon nanotubes and improving their dispersion and compatibility in pressure-sensitive glues, which makes the thermal conductivity of pressure-sensitive composite materials significantly improved. When the content is 10 wt%, the thermal conductivity of the PHBE-MWNT pressure-sensitive composite material is 0.6975 W/(m-K), which is MWNTs 1.8 times the pressure-sensitive glue, which is about 255% higher than the pure pressure-sensitive glue. At the same time, the effects and antibacterial mechanisms of nanosilver on the antibacterial effects of the drug-resistant bacteria Gra04 of aspergillosis AF293 and aspergillosis were studied. The nanosilver produced in this paper has excellent sterilization effects on both AF293 and Gra04. In particular, 8.08×10^{-5} mol/L and 4.03×10^{-5} mol/L nanosilver has a 100% bacteriological rate of both, indicating that the growth of all fungal spores can be completely inhibited. Through DIC microscope observation, nanosilver causes protein denaturation by destroying the proteins in spores, further causing the rupture of cell walls and cell membranes.

Data Availability

Data sharing is not applicable to this article as no new data were created or analyzed in this study.

Conflicts of Interest

The authors state that this article has no conflict of interest.

References

[1] W. Zhao, X. Xie, G. Li, J. Geng, M. Bao, and M. Wang, "Research on the influence of nanocarbon/copolymer SBS/rubber powder composite modification on the properties of asphalt and mixtures," *Advances in Materials Science and Engineering*, vol. 2020, 16 pages, 2020.

[2] G. Wang, W. Shan, S. Wen, Z. Sun, and S. Zheng, "Synthesis of a novel nanocomposite adsorbent for removal of Cr(VI) from wastewater," *Journal of Environmental Sciences*, vol. 57, no. 7, pp. 62–71, 2017.

[3] A. Pal, M. P. Sk, and A. Chattopadhyay, "Conducting carbon dot-polypyrrole nanocomposite for sensitive detection of picric acid," *ACS Applied Materials & Interfaces*, vol. 8, no. 9, pp. 5758–5762, 2016.

[4] J. L. Jiang, X. Zhang, J. F. Du, Q. Wang, J.-F. Dai, and Z.-Q. Wei, "Electrochemical deposition and field emission properties of graphene/diamond-like carbon nanocomposite films," *Acta Physico-Chimica Sinica*, vol. 32, no. 7, pp. 1839–1843, 2016.

[5] H. L. Xu and W. D. Zhang, "Graphene oxide–MnO_2 nanocomposite-modified glassy carbon electrode as an efficient sensor for H_2O_2," *Chinese Chemical Letters*, vol. 28, no. 1, pp. 143–148, 2017.

[6] H. T. Hien, H. T. Giang, T. Trung, and C. Van Tuan, "Enhancement of biosensing performance using a polyaniline/multiwalled carbon nanotubes nanocomposite," *Journal of Materials Science*, vol. 52, no. 3, pp. 1694–1703, 2017.

[7] M. Amir, M. M. Tunesi, R. A. Soomro, A. Baykal, and N. H. Kalwar, "Sensitive determination of 6-thioguanine using caffeic acid-functionalized Fe3O4 nanoparticles as an electrochemical sensor," *Journal of Electronic Materials*, vol. 47, no. 4, pp. 2198–2208, 2018.

[8] F. Cao, C. Li, M. Li, H. Li, and B. Yang, "ZnO nanorod/multiwalled carbon nanotube nanocomposite for ethanol vapour detection," *Micro & Nano Letters*, vol. 13, no. 6, pp. 779–783, 2018.

[9] W. Thomas, C. Sarsons, C. M. Platnich et al., "Maltol-functionalized Fe_3O_4 nanoparticles as T2 magnetic resonance imaging contrast agents," *ChemistrySelect*, vol. 1, no. 8, pp. 1602–1606, 2016.

[10] J. Nelis, D. Migliorelli, S. Jafari et al., "The benefits of carbon black, gold and magnetic nanomaterials for point-of-harvest electrochemical quantification of domoic acid," *Microchimica Acta*, vol. 187, no. 3, pp. 1–11, 2020.

[11] L. Ma, Y. Liu, L. Liu et al., "Simultaneous activation of short-wave infrared (SWIR) light and paramagnetism by a functionalized shell for high penetration and spatial resolution theranostics," *Advanced Functional Materials*, vol. 28, no. 6, pp. 1705057–1705194, 2018.

[12] J. N. B. W. B. Liu and J. L. Shi, "Chemical design and synthesis of functionalized probes for imaging and treating tumor hypoxia," *Chemical Reviews*, vol. 117, no. 9, pp. 6160–6224, 2017.

[13] X. Zou, Z. Wei, J. Du, X. Wang, and G. Zhang, "Preparation and properties of magnetic-fluorescent microporous polymer microspheres," *Chemical Research in Chinese Universities*, vol. 34, no. 4, pp. 684–690, 2018.

[14] Y. Li, J. Liu, Y. Fu, Q. Xie, and Y. Li, "Correction to: Magnetic-core@dual-functional-shell nanocomposites with peroxidase mimicking properties for use in colorimetric and electrochemical sensing of hydrogen peroxide," *Microchimica Acta*, vol. 186, no. 7, pp. 1–9, 2019.

[15] A. Modi, S. Singh, and N. Verma, "Improved performance of a single chamber microbial fuel cell using nitrogen- doped polymer-metal-carbon nanocomposite-based air-cathode," *International Journal of Hydrogen Energy*, vol. 42, no. 5, pp. 3271–3280, 2017.

[16] A. Murray, K. Skene, and K. Haynes, "The circular economy: an interdisciplinary exploration of the concept and application in a global context," *Journal of Business Ethics*, vol. 140, no. 3, pp. 369–380, 2017.

[17] F. M. Shimizu, A. M. Pasqualeti, F. R. Todo et al., "Monitoring the surface chemistry of functionalized nanomaterials with a microfluidic electronic tongue," *ACS Sensors*, vol. 3, no. 3, pp. 716–726, 2018.

[18] G. Wu, A. Santandreu, W. Kellogg et al., "Carbon nanocomposite catalysts for oxygen reduction and evolution reactions: from nitrogen doping to transition-metal addition," *Nano Energy*, vol. 29, no. 1202, pp. 83–110, 2016.

[19] G. Tian, W. Wang, Z. Li, Y. Kang, and A. Wang, "From spent dye-loaded palygorskite to a multifunctional palygorskite/carbon/Ag nanocomposite," *RSC Advances*, vol. 6, no. 48, pp. 41696–41706, 2016.

[20] J. C. Lin, "Radio-frequency radiation safety and health: a research program on the human impact of the wireless telecommunications and other electromagnetic-field-emitting systems," *Ursi Radio Science Bulletin*, vol. 77, no. 4, pp. 107-108, 2017.

[21] S. A. Qasmi, S. Pirzada, A. Ghani, and S. Mohsin, "Survey on proper and safe use of biological safety cabinets (BSCs) in research, bio-medical and animal laboratories in Karachi, Pakistan a cross sectional study," *Journal of Biosafety and Biosecurity*, vol. 2, no. 2, pp. 77–80, 2020.

[22] I. Rai, R. K. Bachheti, C. K. Saini, A. Joshi, and R. S. Satyan, "A review on phytochemical, biological screening and importance of wild apricot (Prunus armeniaca L)," *Oriental Pharmacy & Experimental Medicine*, vol. 16, no. 1, pp. 1–15, 2016.

[23] Y. Zheng, K. Wang, J. Zhang et al., "Simultaneous quantitative detection of helicobacter pylori based on a rapid and sensitive testing platform using quantum dots-labeled Iimunochromatiographic test strips," *Nanoscale Research Letters*, vol. 11, no. 1, p. 62, 2016.

[24] Q. P. Yang, M. Ouyang, G. Y. Yang et al., "Research on ecological stoichiometry in bamboos: from biological basis to applications in silviculture of bamboo forests," *Chinese Journal of Plant Ecology*, vol. 40, no. 3, pp. 264–278, 2016.

[25] S. Duan and C. Juan, "Research on the relationship between sports media and the healthy development of football industry: a case study in Spain football club Real Madrid," *Journal of Computational and Theoretical Nanoscience*, vol. 13, no. 3, pp. 2187–2192, 2016.

[26] B. Gao, X. Ning, and P. Xing, "Shock wave induced nanocrystallization during the high current pulsed electron beam process and its effect on mechanical properties," *Materials Letters*, vol. 237, no. 15, pp. 180–184, 2019.

[27] P. Wang, S. Wang, X. Zhang et al., "Rational construction of CoO/CoF_2 coating on burnt-pot inspired 2D CNs as the battery-like electrode for supercapacitors," *Journal of Alloys and Compounds*, vol. 819, p. 153374, 2019.

[28] Y. Tang, Z. Chen, W. Feng, Y. Nong, C. Li, and J. Chen, "Combined effects of nano-silica and silica fume on the mechanical behavior of recycled aggregate concrete," *Nanotechnology Reviews*, vol. 10, no. 1, pp. 819–838, 2021.

[29] P. Wang, T. Yao, Z. Li et al., "A superhydrophobic/electrothermal synergistically anti-icing strategy based on graphene composite," *Composites Science and Technology*, vol. 198, article 108307, 2020.

[30] L. Zeng, J. Shi, J. Luo, and H. Chen, "Silver sulfide anchored on reduced graphene oxide as a high -performance catalyst for CO_2 electroreduction," *Journal of Power Sources*, vol. 398, pp. 83–90, 2018.